Lab on a Chip

ROYAL SOCIETY OF CHEMISTRY

PAPER

View Article Online
View Journal | View Issue

Check for updates

Cite this: *Lab Chip*, 2025, **25**, 6004

Open Access Article. Published on 10 October 2025. Downloaded on 6/28/2026 1:02:36 PM. This article is licensed under a Creative Commons Attribution 3.0 Unported Licence.

High-resolution time-lapse imaging of droplet-cell dynamics *via* optimal transport and contrastive learning

Luca Johannes Schlotheuber,†[a] Michael Vollenweider, †[b] Sven Gutjahr,†[b] Tiago Hungerland,†[b] Richard Danis,†[b] Weronika Ormaniec,†[b] Aline Linder,[a] Valentina Boeva,*[bcd] Ines Lüchtefeld *[a] and Klaus Eyer *[ae]

Single-cell analysis is essential for uncovering heterogeneous biological functions that arise from intricate cellular responses. Here, microfluidic droplet arrays enable high-throughput data collection through cell encapsulation in picoliter volumes, and the time-lapse imaging of these arrays further reveal functional dynamics and changes. However, accurate tracking of cell identities across time frames with large intervals in between remains challenging when droplets move significantly. Specifically, existing machine learning methods often depend on labeled data or require neighboring cells as reference; without them, these methods struggle to track droplets and cells across long distances within images with complex movement patterns. To address these limitations, we developed a pipeline that combines visual object detection, feature extraction *via* contrastive learning, and optimal transport-based object matching, minimizing the reliance on labeled training data. We validated our approach across various experimental and simulated conditions and were able to track thousands of water-in-oil microfluidic droplets over large distances and long intervals between frames (>30 min). We achieved high precision in previously untraceable scenarios, tracking 50 pl droplets in images with small, medium and large movements (corresponding to ~126, ~800 and ~10 000 μm, respectively) with a success rate of correctly tracked droplets of >90% for average movements within 2–12 droplet diameters, and >60% for average movements of >100 droplet diameters. This workflow lays the foundation for the tracking of droplets over time in these arrays when large and complex movement patterns are present and where the uniqueness of the sample makes repeated experiments infeasible.

Received 11th April 2025,
Accepted 12th September 2025

DOI: 10.1039/d5lc00351b

rsc.li/loc

Introduction

In recent years, the range of single-cell technologies has grown tremendously, allowing researchers to study cellular populations through the lens of heterogeneity and plasticity, discovering new types and functions of cells. While much work has been done on the genomic and transcriptomic level, DNA and RNA by themselves are often a poor descriptor of activity and functionality, both of which are often best assessed directly. Moreover, the time component of activity and function is essential in its analysis as cells might display dynamic plasticity and functional changes over time.

Therefore, the direct analysis and dynamic tracking of cells is often a necessity in various biological applications *in vivo*,[1,2] *ex vivo* in lab-on-a-chip devices[3] and in droplet-based systems.[4] Indeed, droplet-based microfluidics have emerged as potentially transformative tools with many applications in modern medicine and fundamental science.[5–8]

While the analysis in droplet microfluidics often focuses on a selected time point, a subset of droplet microfluidics, 2D droplet microfluidics, has further emerged as an interesting proposition to study cellular functionalities dynamically, allowing for the discrimination of sequential and simultaneous functionalities, cellular plasticity, cell–cell interactions, and fate.[9,10] In practice, 2D single-cell analysis relies on the separation of cells in droplets, their arrangement into arrays, and the measurement over time in different channels to visualize features/functionalities in large composite images to achieve sufficient throughput to

---

[a] *Laboratory for Functional Immune Repertoire Analysis, Institute of Pharmaceutical Sciences, Department of Chemistry and Applied Biosciences, ETH Zürich, Zürich, Switzerland*
[b] *Department of Computer Science, ETH Zürich, Zürich, Switzerland*
[c] *ETH Al Center, ETH Zurich, Zurich, Switzerland*
[d] *Swiss Institute of Bioinformatics, Lausanne, Switzerland*
[e] *Department of Biomedicine, Aarhus University, Bartholinbygningen, Wilhelm Meyers Alle 4, 8000 Aarhus C, Denmark. E-mail: eyerk@biomed.au.dk*

† Contributed equally.

This journal is © The Royal Society of Chemistry 2025

Open Access Article. Published on 10 October 2025. Downloaded on 6/28/2026 1:02:36 PM.
This article is licensed under a Creative Commons Attribution 3.0 Unported Licence.

detect rare events or gather enough data for reliable downstream analysis.[11–14]

Here, a balance needs to be struck between the throughput, *i.e.*, the size of the imaged array and, therefore, the number of cells, the necessary time resolution and the dynamics of the cellular process, which sometimes needs hours/days to complete. Therefore, individual frames are often a few minutes apart, while shorter imaging intervals might lead to excessive bleaching, reduced numbers of imaged cells and unnecessary large data sets. With the growing demand for larger-scale and deeper analytical resolution (100 000 events with multiple measured parameters in parallel), time intervals between data points might further increase.

Whereas small movement and rearrangements resulting in a droplet shift below 1/2 the droplet diameter can be easily tracked using the droplets centroid between time frames, correct tracking becomes difficult if droplets displacements are larger than their radius, as the droplet centroid of the previous time-point cannot be used as the main reference point with certainty. Tracking through signal (inside cells or droplets) remains also problematic as it requires a biological understanding (and prediction) of how the signal will develop. In addition, potential non-uniform changes in cellular activity complicate this approach. Although various tracking algorithms have been developed in adjacent applications, they often depend on visual cues or relative positioning with respect to neighboring cells/droplets for accurate analysis.[15,16] These approaches are tailored for (machine) learning, object recognition, and tracking of specific cell types; how ever, benchmarking video datasets from cell tracking challenges, such as FluoN2DL-Hela, typically cover only 5–15 μm of movement per frame at 30-minute intervals. Secondly, these methods are optimized for small image sizes (1–5 millimeter).[16,17] In contrast, our data represents merged images of 10 × 10 field of views (>10 mm) that cover between 20–80 000 droplets and traveled distances between 50 and 500 μm. This data is therefore considerably more challenging compared to other applications.

Recent work has explored diverse approaches to droplet tracking and microfluidic flow analysis, ranging from classical models to modern deep learning. For instance, Bogdan *et al.*[18] investigated stochastic jetting and droplet motion in confined granular flows, highlighting the unpredictable displacements that complicate object correspondence-an issue our method is designed to address. Similarly, Gai *et al.* characterized the collective behavior of crowded droplets in microfluidic systems,[19] underscoring the importance of population-level interactions that often produce non-local motion. On the machine learning side, Durve *et al.* benchmarked YOLOv5/YOLOv7 with DeepSORT for droplet tracking,[20] offering an effective approach for structured or labeled settings. However, such architectures often rely on clear inter-object differences or persistent visual features, which are absent in our high-density, label-free droplet arrays. Our framework overcomes these limitations by combining unsupervised visual embed dings and unbalanced optimal transport, enabling robust trajectory reconstruction even under large displacements and ambiguous visual conditions.

Here, in this application, additional challenges are posed (i) by the high optical similarity in droplet arrays, (ii) potentially large and complex movement patterns without preserving local structures, (iii) large time intervals between images, and (iv) the lack of physical boundaries, meaning that droplets could enter and exit between frames. Recently developed or commercially available software struggles to resolve such data.[4,21]

Often, researchers opt to repeat experiments if large and uncontrolled movement is detected. Although experiments with cell lines can be redone, this is not feasible for rare, sensitive, or unique samples. Here, inaccurate tracking could lead to incorrect assignments and producing false conclusions. Only when cells are correctly tracked and data assigned do these techniques enable the accurate extraction and resolution of relevant data. Therefore, novel algorithms are needed to allow for the successful tracking of cellular functionality when movement is present in these arrays.

This study introduces a novel approach for processing over-time droplet experiments. Our approach integrates positions and visual representations of the droplets into an optimal transport (OT) algorithm to enable effective tracking of the droplets across space and time independent of the potential signals. The pipeline we present consists of (i) a pre-processing, (ii) a droplet detection, (iii) a visual feature extraction, and (iv) finally a matching and uncertainty quantification step (Fig. 1). The pipeline further includes a tool to visualize individual predicted trajectories with their respective certainty levels. We evaluated the visual feature extraction and showed that our model produced meaningful features for tracking the droplets, which stayed consistent over time. Next, we evaluated the full pipeline heuristically on real data and quantitatively on simulated data. Finally, we linked the algorithm to a read-out algorithm that calculated fluorescent mean intensities, which we used to track color-coded droplets across time and space and verified the predicted trajectories (Fig. 1).

To illustrate the usefulness of this approach, we present in this paper data from a mouse immunization study. In this study, a small subset of data sets showed increased movement, only allowing to extract data from a fraction of droplets. Due to the nature of the samples, *i.e.*, they cannot be conserved, and the comparison between mice it was not possible to repeat these measurements without immunizing a new set of mice, which comes with its own ethical and scientific implications.

Methods

Experimental time-lapse imaging data

For experimental data, we used time-lapse epifluorescence images comprised of up to 6 different channels and 100 field

Open Access Article. Published on 10 October 2025. Downloaded on 6/28/2026 1:02:36 PM.
This article is licensed under a Creative Commons Attribution 3.0 Unported Licence.

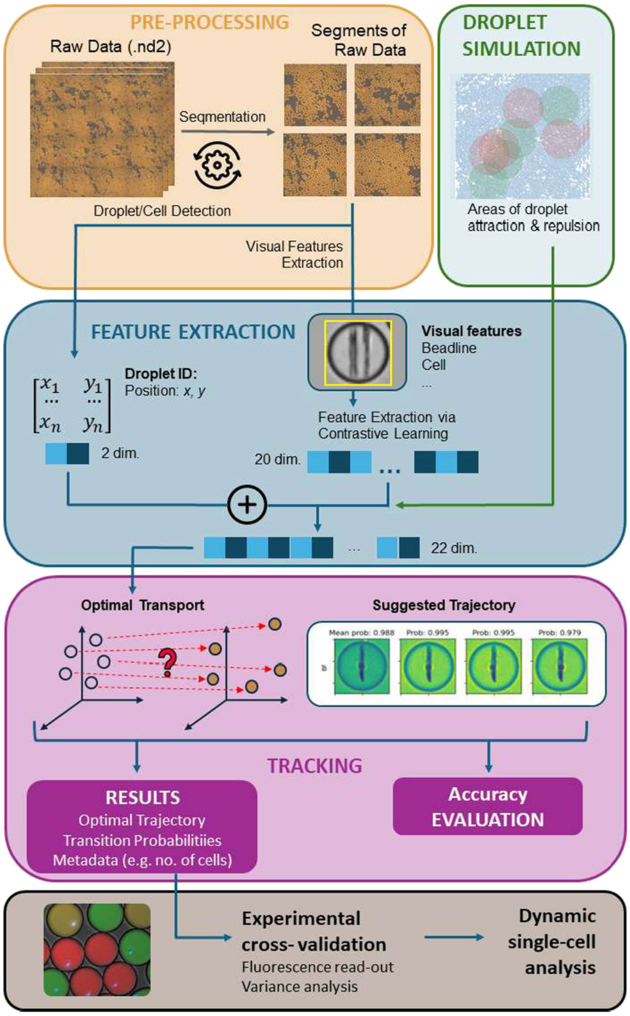

Fig. 1 The main pipeline of data analysis from pre-processing to trajectory generation. Raw data was segmented and visual features extracted. Simulation modeling was performed to validate labeling and accuracy during (droplet population) movement. Different types of movement were simulated, areas of attraction (droplets moving towards one position) and repulsion (droplets moving away). Droplets were tracked using optimal transport (OT) implementation and trajectories of individual droplets generated, lastly from fluorescent droplets that enabled their cross-validation.

of views (10× objective), which were merged to a consecutive image spanning roughly 6 × 6 or 10 × 10 mm. Generally, the data was acquired every 15, 30 or 60 minutes and contained between 5 and 15 intervals (Fig. 2). We used two experimental data sets, one already published and one specifically generated. Specifically, dataset 1 included experiments for the detection of cytokines from peripheral blood mononuclear cells (PBMCs) after stimulation.[22] including a nanoparticle-based detection bioassay, further described in literature.[4,9] From this set, four experiments were run, differing in their total movement (based on Earth mover's distance, EMD), ranging from small to large movement. The 2nd set of experiments, dataset 2, consisted of images with droplets with Chinese Hamster Ovarian (CHO) cells (Eurofins) without added nanoparticles, produced using a microfluidic chip as described previously.[9,22] For dataset 2, no adaption or fine-tuning of the contrastive learning or OT-problem balancedness was performed. Technical replicates with low-to-medium and large movements were performed from this data, referred to as biological cross-validation dataset. An overview of the acquired and used datasets can also be found in Table 1.

Simulated data

Following our observations on experimental data, we simulated trajectories reflecting three different types of motion: divergence spots (droplets had a tendency to move away from red circles), attraction spots (droplets had a tendency to move into green parts), and big droplets that moved at large speed through the image. To acquire the droplets' visual features, we used a data set of already tracked droplet trajectories and paired them with the simulated locations. Details of how the simulated data was integrated into the pipeline can be found in the SI I and visualized in Fig. S1; simulated data are available at **https://github.com/ls154/DropletTracking/**.

Pre-processing and object detection

Pre-processing involved image segmentation and subsequent droplet and cell detection. Large time-lapse image files (>10 GB) can strain computational resources; thus, we implemented an optional step to segment frames into disjoint segments, reducing memory requirements. First, we translated and implemented in Python the cell- and droplet detection algorithms from a previous application[4] to create an end-to-end pipeline importing all necessary parameters for optimal transport (OT)-based tracking. Specifically, we provided the option to detect droplets in the preprocessed bright-field channel using a combination of the Hough circles algorithm[23] and the RANSAC (Random sample consensus) algorithm.[24] To avoid false-positives, droplets exiting image boundaries after measurement (in between time intervals) were not considered for tracking, while droplets entering were added continuously to the pipeline. A more detailed de scription can be found in SI II and Fig. S2.

Visual feature extraction *via* contrastive learning

To incorporate visual features in the droplet tracking, we trained a convolutional neural network (CNN) to learn a low-dimensional vector representation of each droplet. As the CNN encoder backbone, we chose an EfficientNet-B1 model[25] due to its optimal features balanced between computational size of the model, accuracy, and efficiency which was further finetuned.[26] The input to the encoder were droplet images of size 40 × 40 pixels (*i.e.*, containing one droplet) with 2 channels, the preprocessed bright-field and cell detection channel (here, DAPI using CellTrace Violet, ThermoFisher). Finally, the output of the CNN embedding droplet images was a 20-dimensional feature vector:

Open Access Article. Published on 10 October 2025. Downloaded on 6/28/2026 1:02:36 PM.
This article is licensed under a Creative Commons Attribution 3.0 Unported Licence.

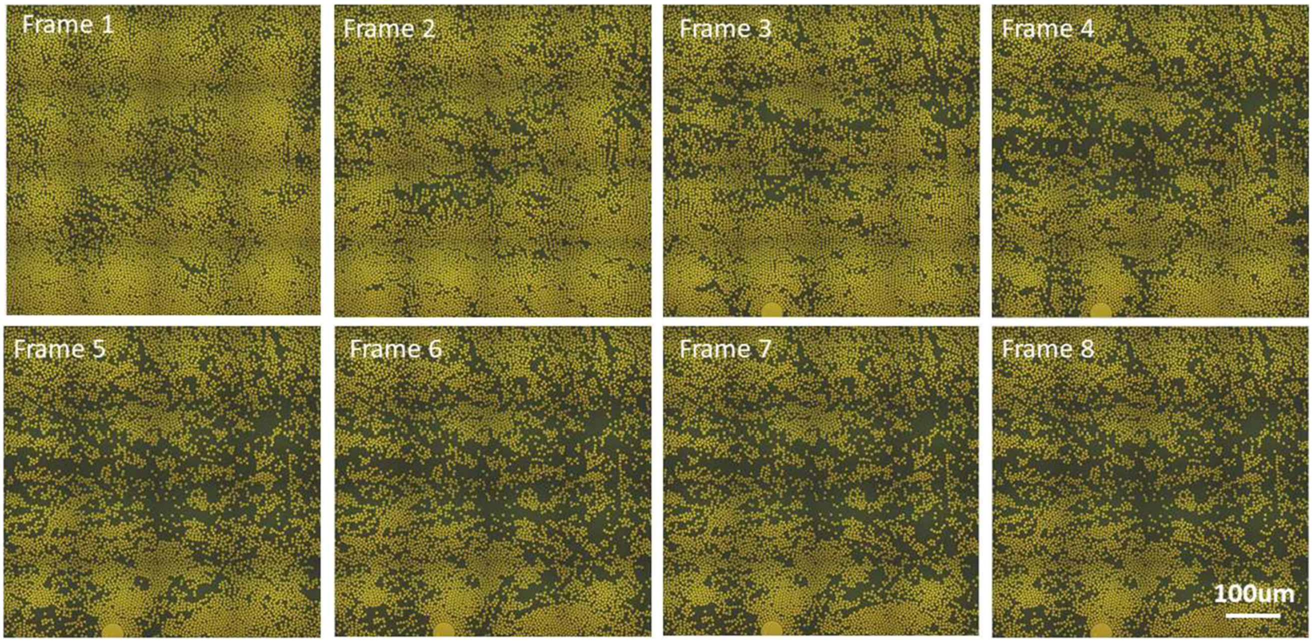

Fig. 2 Visualization of example raw data from large-scale fluorescent micro fluidic droplet experiments assayed at different time-points (frames). Varying degree of droplet movement (and thus cells contained inside) is visible between each frame increasing over-time.

Table 1 Overview of experiments and datasets used in this study

Datasets	Type	Droplet content	Application	Used for
Dataset 1	Experimental	Beadline and PBMCs	Cytokine secretion	Experimental validation and tuning
Dataset 2	Experimental	CHO cells	Cell reporter	Cross-validation
Dataset 3	Simulated	Beadline and PBMCs	Simulating/modeling movement	Labeling validation and accuracy analysis
Dataset 4	Experimental	Beadline and PBMCs	Proof-of-concept	Proof-of-concept

$$f_{\text{enc}}\colon \mathbb{R}^{40\times40\times2} \to \mathbb{R}^{20}. \tag{1}$$

To produce meaningful representations, we used a contrastive learning approach to induce closeness in the latent space of two droplets from the same trajectory, while increasing distance in the latent space of two droplets from different trajectories. For this purpose, we employed the InfoNCE loss function for a batch of representations Z as follows:[27]

$$\mathcal{L}_{\text{InfoNCE}}(\mathcal{Z}) = -\sum_{i=0}^{N}\log\frac{\exp\left(z_{i,t}{}^{\top}z_{i,t+1}/\tau\right)}{\sum_{k=1}^{N}\exp\left(z_{i,t}{}^{\top}z_{k,t+1}/\tau\right)}. \tag{2}$$

Here, $z_{i,t} = f_{\text{enc}}(x_{i,t})$ denotes the learned representation of droplet i at time step t, N is the batch size and T is the temperature parameter controlling the shape of the resulting distribution. The corresponding process is illustrated in SI III, Fig. S3, where $x_{i,t}$ is called the anchor, $x_{i,t+1}$ the positive and $x_{j,t+1}$, $j \neq i$ are negative representations. We used an EfficientNet-81 architecture pretrained on ImageNet as the encoder backbone.[25] The embedding dimension was set to 20. The network was trained using the Adam optimizer (learning rate 0.001, batch size 128) for 50 epochs. Training data consisted of 30 000 positive droplet pairs derived from low-movement sequences, and validation used an additional 30 000 disjoint pairs. The InfoNCE loss was used to bring together embeddings of temporally adjacent droplets while repelling others within the batch.

Implementation of the OT algorithm for droplet tracking

In simple terms, OT tracking addressed the question of how to best transport a given source "mass" (droplet population) to a target mass (droplets in next frame).[28,29] We solved the actual OT problem, also known as the fully unbalanced entropic regularized OT problem, using a slightly modified version of the commonly used Sinkhorn algorithm.[30] The input to OT was a cost matrix $C \in R^{n\times m}$ in our case, C represented the cost of transporting a source droplet to a target droplet. The output of OT between two consecutive frames was a transport plan $T \in R^{n\times m}$, where n and m were the number of droplets in the source and target frames, respectively. The transport plan captured which droplets were supposed to be matched, with each entry $T_{i,j}$ indicating how much mass was transported from the i-th droplet in the source to the j-th droplet in the target frame. This problem resulted in the following optimization objective:

Open Access Article. Published on 10 October 2025. Downloaded on 6/28/2026 1:02:36 PM.
This article is licensed under a Creative Commons Attribution 3.0 Unported Licence.

$$\min_{T\in\mathbb{R}_+^{n\times m}}\langle T, C\rangle. \tag{3}$$

We designed a cost function that combined a positional loss and a visual embedding loss, according to:

$$C_{i,j} = \alpha L_{\text{pos}}(x_i, y_j) + (1 - \alpha)L_{\text{vis}}(x_i, y_j), \tag{4}$$

where L_{pos} and L_{vis} are the positional and visual embedding losses, a is a hyperparameter that determined the relative importance of each loss, and x_i and y_i represent the ith droplet in the source frame and the jth droplet in the target frame. More details on the encoder hyperparameter and metrics for encoder evaluation can be found in the SI IV and Table S1. Specifically, each loss was defined as follows:

$$L_{\text{pos}}(x_i, y_j) = ||x_i^{\text{pos}} - y_j^{\text{pos}}||_2 \tag{5}$$

$$L_{\text{vis}}(x_i, y_j) = ||x_i^{\text{vis}} - y_j^{\text{vis}}||_2 \tag{6}$$

Further, we scaled the positional loss as such that the 95-quantile of the loss was numerically equivalent to the 95-quantile of the visual embeddings loss, making the interpolation between the two losses meaningful and controllable. In order to implement the basic OT function, two challenges had to be addressed. First, eqn (4) had infeasible computational complexity, and second, the possibility of losing or gaining mass between frames had to be accounted for. To alleviate these two issues, the objective was modified to include entropy regularization for efficiency in eqn (3). Since droplets entered or left the frame, the number of droplets in the source and target frame might not be the same making the problem unbalanced. Since, in this case, not all droplets could be transported to the target frame at all times, this required computational adaption.[31] Thus, Kullback–Leibler (KL) divergence terms were introduced to relax the balancedness constraints yielding the final objective as followed:

$$\min_{T\in\mathbb{R}_+^{n\times m}}\langle T, C\rangle + \rho_{\text{a}}\text{KL}\left(T1_m||\frac{1}{m}1_m\right) + \rho_{\text{b}}\text{KL}\left(T^{\text{T}}1_n||\frac{1}{n}1_n\right) - \in E(T) \tag{7}$$

where 1_k is the all ones vector of dimension k, while ρ_{a} and ρ_{b} control the amount of 'slack' allowed in the balancedness of the problem. ρ_{a} controls balancedness of the source distribution and ρ_{b} the target distribution, respectively. Here, high values enforced a stricter control and balance of masses while lower values allowed for 'slack' in the conservation of masses. $E(T)$ was defined as the entropy-regularizer of T:

$$T\left(E(T) = \sum_{i,j} T_{i,j}\log T_{i,j}\right) \tag{8}$$

which controls smoothness and spread of transport matrices, encouraging more distributed or less sparse assignment of masses. Furthermore, the regularization parameter E controlled the regularization strength and influenced how 'willing' a given source point is to share its mass with multiple points of the target distribution rather than just transporting all its mass to a single point. We used a combined cost function with a weighting parameter a, balancing spatial distance and visual similarity. Based on a parameter search, we selected $a = 0.5$ for most conditions. Entropy regularization was set *via* $\varepsilon = 0.005 \times \text{mean(C)}$, and KL penalties for source and target distributions were set to $\rho_{\text{a}} = \rho_{\text{b}} = 0.999$ for low/medium movement and 0.99 for high movement. These parameters were chosen to optimize tracking precision and stability, particularly under unbalanced conditions with entering/exiting droplets. Sensitivity plots for these hyperparameters are available in SI V, Fig. S4.

Trajectory generation

Lastly, we estimated trajectories for all droplets across all time steps using the solutions to the OT problem. The droplet detection mechanism assigned each droplet i in the source and j in the target mass unique IDs, d_i^{s} and d_j^{t}, respectively. When a target droplet received the most mass from a given source droplet, we considered this as a match, receiving the same 1D as the source droplet. The IDs were later used to produce trajectories. Thus, the tracking assignment rule was defined as follows:

$$d_{\gamma(i)}^{\text{t}} \leftarrow d_i^{\text{s}} \text{ for } \gamma(i) := \arg\max_{k\in\{1,\ldots,m\}} T_{i,k}. \tag{9}$$

The transported mass, quantified by $s_i = T_{i,\gamma(i)}$, indicates the certainty of the tracking of droplet i in the source to droplet $\gamma(i)$ in the target frame. To increase the interpretability of the transport mass, we linearly scaled all entries in the OT matrix onto the range [0, 1] before applying eqn (9) to obtain s_i, which provided an adequate approximation for confidence levels. To adjust s_i to represent true probabilities from which the confidence can be obtained directly, we calibrated s_i as described in the SI VI. Using the matching rule (eqn (9)) for all droplets and all frames of a time-lapse series, the trajectories of all droplets present in the first frame were predicted. If two source droplets were (theoretically) transported to the same target droplet, the droplet with lower amount of transported mass was removed and the corresponding trajectory filtered out.

Getting labeled data for CNN fine-tuning

In order to get data with high confidence, we employed a heuristic approach by only considering a subset of droplets from a droplet array with visually little to no movement. Specifically, only droplets with less than 5 pixel (6.5 μm, less than 1 droplet radius) of moved distance between frames were included as labeled data. We validated this approach by manually checking the tracking results for a subset of droplets. This heuristic was used on a collection of 7 time-

Open Access Article. Published on 10 October 2025. Downloaded on 6/28/2026 1:02:36 PM.
This article is licensed under a Creative Commons Attribution 3.0 Unported Licence.

lapse series. By doing so, we extracted 30 k droplet pairs for training and another 30 k droplet pairs for validation. To test the final model, we employed a databank of about 13 k human-labeled pre-collected trajectories. This dataset is referred to as dataset 3.

Movement, classification and time resolution

In order to independently evaluate the degree of total movement before tracking (from both experimental and simulated data), we calculated the Earth-Mover Distance (EMD). The EMD quantified the "cost" of moving all objects be tween two time points by summing the total observed distance. To calculate the EMD, the input image was dimensionally reduced and treated as a single entity. The output EMD profile displayed the movement for each interval and median across the whole series, and we calibrated the EMD metric against the actual distance (in pixel per μm) of average droplet movement in a separate image series, where a defined movement was introduced computationally (see also SI VII). All images were classified based on their EMD/distance into low, low-to-medium, medium and large movement. Acquired experiments in dataset 2 were taken at 1–2 min intervals to produce data that approximated labeled (ground truth) data, also referred to as "high-temporal resolution". Such images required acquisition with lower field of views (2–4 mm) in order to acquire the image. Generally, this allowed droplet tracking based on consecutive (droplet) centroid positions alone, which was validated using a previously available software.[4] From this data, longer time intervals were generated by removing frames, generating time-lapse series with intervals of 5 min, 15 min, and 30 min for direct comparison, further mimicking more common experimental settings[22] in a controllable manner.

Measuring tracking failure using fluorescent droplet barcodes

In dataset 2, droplets contained fluorescent barcodes that allowed to identify certain subpopulations. Different dyes were encapsulated separately and mixed prior to acquisition, creating surrogates for evaluating correct trajectories. We added a Python code for reading out barcode intensities of droplets and cells by storing maximum, mean, and median fluorescent intensities. Taking the generated trajectories (x, y per time-point), we calculated the droplet fluorescent intensity around the estimated droplet position for each droplet, channel and time point, respectively. Fluorescent barcode changes were calculated for each droplet-time transition (time point T_x compared to T_{x-1}). A droplet was denoted "falsely tracked" if the intensity change was larger than 20% of the intensity distribution of all barcodes at T_0. This metric then allowed to quantify the frequency of incorrectly tracked events per time interval. Raw data read-out for trajectory evaluation are shown in SI VIII.

Immunization and droplet measurements of murine adaptive immunity

BALB/c mice (Janvier Labs, female and male, age 8–10 weeks at the start of the protocol) were immunized intraperitoneally and the extracted cells processed as described elsewhere.[4,34,35] All animal procedures were performed in accordance with local policy and the respective Swiss law and ordinances, and were approved by the Cantonal ethics committee of Zurich under license number ZH215/19.

Results

Validation of visual embeddings

First, we investigated the question whether we could only track the droplets containing cells, or whether such an approach might work to track all droplets on data sets with minimal movement. We, therefore, first evaluated the visual embedding models on dataset 1, where droplets contained cells and magnetic nanoparticles (beadlines) as visual features (Fig. 2).

Two models were trained: $\text{Mod}_{\text{cells}}$, which was trained exclusively on droplets with cells, and Mod_{all}, which was trained on both droplets with and without cells (Table 2). We compared the effect of both models on the tracking accuracy from a validation set and a held-out test set (Fig. 3). Overall, both models generated meaningful embeddings, allowing for effective droplet matching based on distances in the embedding space. Within the validation set, both models achieved a high top 1 accuracy of 0.952 ± 0.013 and 0.963 ± 0.011, indicating a high rate of correct matches for the nearest predicted droplet in the embedding space.

In the smaller test set (test), they performed similarly well (0.983 ± 0.003 and 0.985 ± 0.02, respectively). In these first tests, we noticed that an increased sample size impacted the accuracy of matching based on distance only marginally, although the task became more difficult. The comparable performances on the validation and test sets from dataset 1 suggested that the models might be capable of generalizing across different time-lapse datasets. Interestingly, Mod_{all}

Table 2 Performance metrics for different models across validation and test datasets. Top 1 and top 5 accuracy as well as area under the ROC curve (mean and its standard error across 9 frames). Number of droplets in the test dataset: 13 584. Metrics are based on Euclidean distance. A detailed description of the metrics can be found in SI IV

Metric	$\text{Mod}_{\text{cells}}$ (val.)	$\text{Mod}_{\text{cells}}$ (test-sub)	$\text{Mod}_{\text{cells}}$ (test)	Mod_{all} (val.)	Mod_{all} (test-sub)	Mod_{all} (test)
TOP 1 ACC	0.952 (0.013)	0.992 (0.002)	0.983 (0.003)	0.963 (0.011)	0.993 (0.001)	0.985 (0.002)
TOP 5 ACC	0.981 (0.008)	0.999 (0.001)	0.996 (0.001)	0.986 (0.006)	0.999 (0.000)	0.997 (0.001)
AUROC	0.988 (0.001)	0.990 (0.000)	0.990 (0.000)	0.988 (0.001)	0.990 (0.000)	0.990 (0.000)

Open Access Article. Published on 10 October 2025. Downloaded on 6/28/2026 1:02:36 PM.
This article is licensed under a Creative Commons Attribution 3.0 Unported Licence.

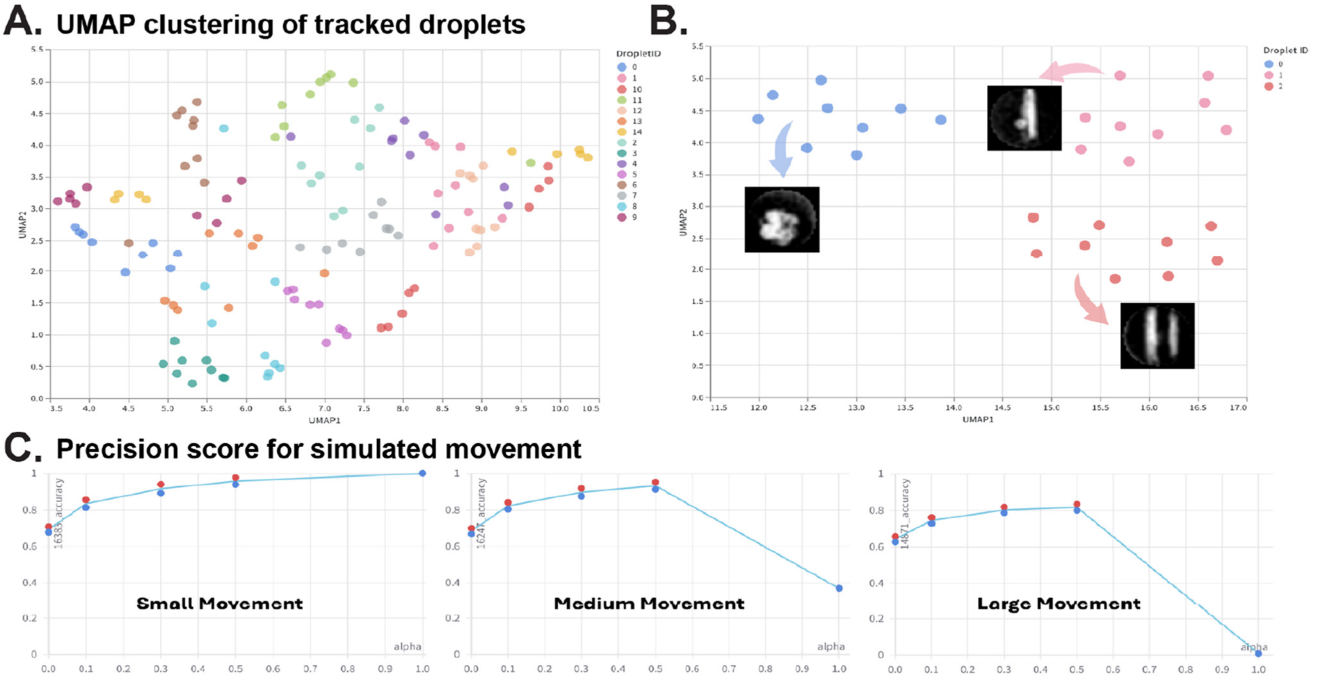

Fig. 3 A. Embeddings of 15 random droplets tracked across 9 frames, reduced with UMAP to visualize tracking clustering performance and colored by their droplet ID. B. Zoom-in on embeddings of three representative droplets with different visual content were tracked across 9 frames. C. Precision score for small, medium and large movement simulations as a function of α. Red and blue dots represent the runs with model 1 and model 2 used for the visual embeddings respectively. Other parameters: $\rho_\alpha = \rho_b = 0.999$ for small and medium movement and $\rho_\alpha = \rho_b = 0.99$ for large movement, $\varepsilon_{\text{rel}} = 0.005$. Embedding space cost defined through Euclidean distance. Corresponding area under precision recall curve (AUPRC) scores for the best performing parameter sets for small, medium and large movement were 1.000, 0.998, 0.987 respectively.

slightly outperformed $\text{Mod}_{\text{cells}}$ on top 1 and top 5 accuracy. As the performance was sufficiently high, we continued with Mod_{all} as the default pipeline as this would also allow us to track all droplets independent of cellular content. Afterward, to assess both the global and local structure of the embedding space, we reduced the embedding dimensionality using both UMAP (Fig. 3) and PCA (SI IX) with nearest neighbors = 15, minimal distance = 0.1, spread = 10. For both dimensionality reduction techniques, we demonstrated that the same droplets, represented by the same-colored points, tended to form clusters according to their visual representation. Visual embedding models were capable of resolving single droplet trajectories based on visual features accurately, exemplified in Fig. 3B. Although these evaluation datasets contained only minimal movement (<50 μm average droplet movement), we concluded that OT-based matching should incorporate visual features for better performance.

Parameter search on simulated data

To quantitatively evaluate the full pipeline and to set the hyperparameters in eqn (7), we used dataset 3 (simulated data), where we could introduce different movements in a controllable manner. Here, we performed a grid search on the regularization term in OT ε_{rel} ($\varepsilon = \varepsilon_{\text{rel}}$ mean(C)), on regularization parameters for adapting to data unbalancedness ρ_α, ρ_b (set to either 0.99 or 0.999), and on the weighting parameter which controls the contribution of location loss to the cost function a. All results can be found alongside tested values in the SI I.

Our simulation had 20 k droplets in each frame, but we cut image boundaries *in silico* to introduce (more realistic) imbalance, leaving about 16 k droplets with some degree of imbalance across different frames representing droplets that might get lost from frame to frame due to their movement. We observed that irrespective of other parameters, the choice of $\in_{\text{rel}}$ did not significantly influence the metrics. Thus, we choose $\in_{\text{rel}} = 0.005$. The choice of $\rho_\alpha = \rho_b = 0.999$ was optimal for small and medium movement data while $\rho_\alpha = \rho_b = 0.99$ was better for large movement. Hence, we fixed these metrics according to this choice and subsequent runs were obtained with these selected parameters (Table 2).

Finally, we studied the precision for all droplets and of the top 10 000 most certain droplet trajectories (10K precision). We clearly observed that bigger values of a worked better for smaller movement, while for medium and large movement taking an alpha of about 0.5 performed best (Fig. 3 and S4). We concluded that for small movement (EMD <0.5), just using the positions was almost sufficient for the OT to work efficiently and as soon as there is more movement we had to include visual information to get high scores.

Within our envisioned applications, we valued that false negatives would be preferred over false positives. Hence, droplet populations successfully tracked should be correct with high confidence even when filtering out droplets that

Open Access Article. Published on 10 October 2025. Downloaded on 6/28/2026 1:02:36 PM.
This article is licensed under a Creative Commons Attribution 3.0 Unported Licence.

could be potentially tracked. Therefore, for the intended use of the algorithm where trajectories with high certainty are provided, we recommend using $\alpha = 0.5$, which yielded almost perfect tracking for 10 k most certain droplets in our experiment, which was more than 50% of the droplets in this series.

Visual evaluation of reported trajectories

We next visualized and validated the droplet trajectories returned by our method from dataset 1 used earlier. Fig. 4 presents a selection of the analysis of a small section of the large droplet array, and the predicted droplet centers are shown as interconnected dots overlaid on the real microscope image from the first step (blue), and the lines provide the trajectory of the center of the droplet (SI X). While some trajectories appeared plausible, such as the one from the droplet in the green box, we could identify mismatches (indicated by the red box), both visually and based on OT-scores. For example, focusing on the droplet in red, a mismatch occurred between the second to the third frame. This discrepancy was evident both in image as well as in the OT transition probability, which dropped to 0.48 during this transition but otherwise stayed above 0.75, as shown by the line-plot below the time series (Fig. 4). We proposed that observed irregularities (red series) could also be identified in the post-tracking analysis visually or by the OT-transition score.

OT-based tracking produces high accuracy and more than 80% increase in trajectory recovery

Next, we wanted to compare the tracking efficiency on droplet arrays that dis played different movement pattern in dataset 1 using different time resolutions in between frames. We applied the previously determined settings on data with 5 min, 15 min, and 30 min time resolution and calculated the percentage of trajectories that could be reliably recovered compared to high-temporal resolution. As a comparison, we used the percentage of droplets that could be tracked using a previously published analysis software,[4] which allows reliable tracking of movement <10 pixels (<13 μm). To compare experiments in terms of total droplet movement (small, medium, and large), we calculated the Earth-Mover distance metric (EMD) for each experiment. The small movement exhibited a median EMD of 0.483, medium movement of 0.895, and large images up to 6.294 (SI VII). We converted the EMD to the average distance moved in μm and droplet diameter to quantify the droplet movement. Here, small movement images demonstrated an average movement of all droplets of 2 droplet diameters (dd), medium of 12 dd and large movement of up to 160 dd, corresponding to ~10 000 micrometers.

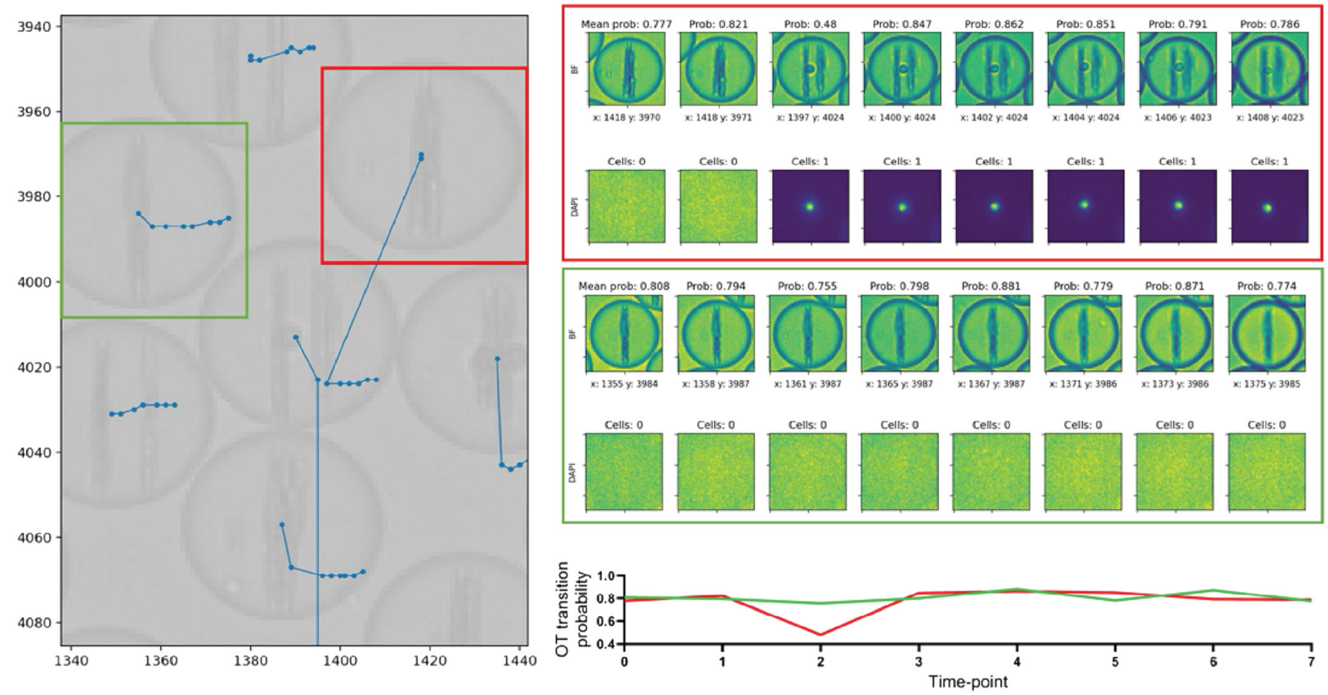

Fig. 4 Overlay of droplet regions with tracking positions from initial tracking analysis of small-movement experiments. Blue dots and lines indicate trajectories over all eight time frames. The background shows the bright-field channel of the first frame. Green bounding box indicates high confidence tracked droplet across time intervals. Red indicates a droplet that was mismatched. Corresponding, extracted bright-field and DAPI channel patches of the green and red droplet trajectories are depicted with optimal transport (OT) probabilities for each time transition to the right. The mean probability of the whole trajectory is included above the first time frame (mean prob.). Information about the detected number of cells is included above the DAPI channel at each time frame as OT transition probability graphed.

Open Access Article. Published on 10 October 2025. Downloaded on 6/28/2026 1:02:36 PM.
This article is licensed under a Creative Commons Attribution 3.0 Unported Licence.

As expected, most droplets were not trackable using our previously described tracking software. Specifically, the analysis resulted in the successful tracking of only 23% of droplets in low-movement images, whereas images with larger movement resulted in complete loss of data (Fig. 5, "trackable by droplet centroid"). To note, the discrepancies in tracked events between medium and large movement (in terms of 0.7% tracked events *versus* EMD) was due to a small subpopulation of droplets moving very little (<10 pixels), while the majority moved larger distances due to non-uniform movement. We observed a stark contrast compared to the solution described in this paper, where most droplets were trackable in all scenarios. In terms of image tracking accuracy, we observed a downward trend in accuracy for trajectories as time resolution decreased (Fig. 5). Nevertheless, we maintained an overall accuracy greater than 0.6 even at 30 minute intervals and for large movements of 160 droplet diameters on average. As discussed earlier, the frequency of droplets where any transition between time-points was above 0.5 OT-scores was 91.6, 99.3 and 61.8% for the different movement types, respectively. A cut-off of 0.5 was chosen according to the OT-score expected, when a trajectory resulted in a false transition (Fig. 4). Thus, the results showed that overall droplet tracking improved from previously 0% to over 60% in high-movement instances. This demonstrated the strength of the pipeline in recovering trajectory data and tracking the droplets successfully. From this analysis, we concluded that even experiments with EMD >2 could be accurately tracked for a substantial proportion of droplets. Notably, the pipeline maintained tracking accuracy above 99% even when droplets were displaced by more than 10x their diameter (~800 μm, Table 3). Even in images with displacement ~10 000 μm displacement (>100× the diameter of one droplet) more than 60% of droplets could be tracked, a regime previously considered intractable for label-free tracking. This ability to recover long-distance trajectories represents a substantial advance over existing methods that fail beyond 5–10 diameters.

Confirmation of tracking success using fluorescence intensity barcodes

To externally validate the resolution at which droplet trajectory can be recovered from time-lapse series, we added fluorescent barcodes into each droplet, consisting of fluorescent-colored dyes, for example, FITC (green) combined with cell staining in DAPI (blue, experimental dataset 2). Here, the fluorescence signal was not used for tracking, but the constant, channel-specific intensity allowed to identify non-correctly tracked droplets in a simple manner. In the case of an incorrect matching, the extracted intensity would

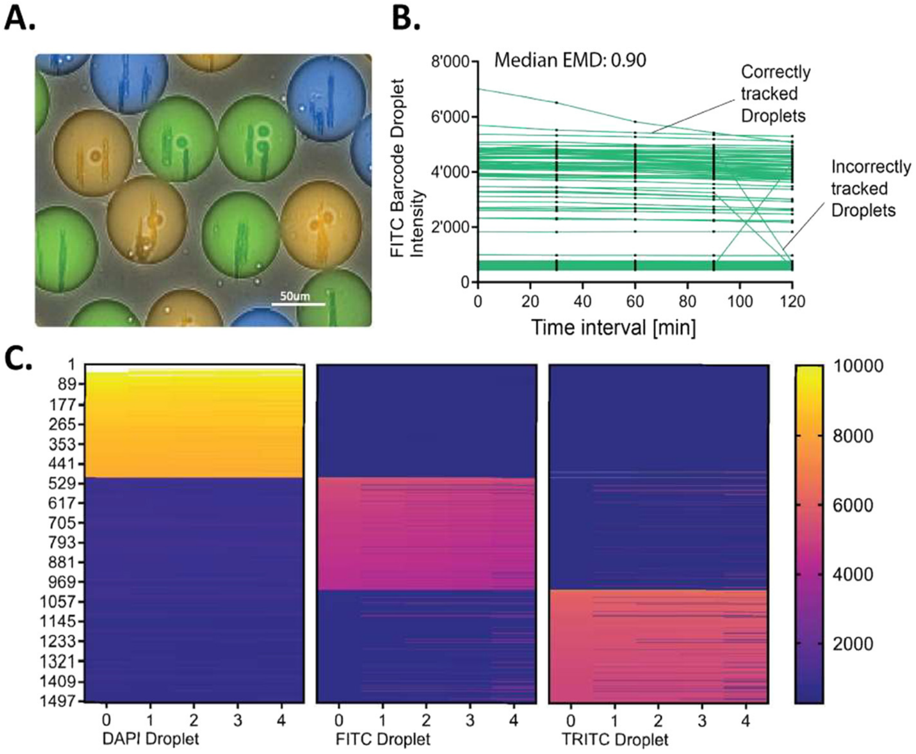

Fig. 5 A. Representative droplet image of barcoded experiments (dataset 2). B. FITC (green) mean fluorescence intensity (MFI) of 500 droplets, picked at random over each time-point for experiments with cells and beadline bioassay. The experiment was characterized as medium movement, and a 30-minute time interval was used. Highlighted are two examples of correctly and incorrectly classified trajectories according to intensity change between intervals. C. Heatmap of individual droplet trajectories of 500 droplet sorted by channel and intensity in descending order. *X*-axis represents time-points (5 time-points) from 30 min interval experiments. Colors indicate fluorescence intensity.

This journal is © The Royal Society of Chemistry 2025

Open Access Article. Published on 10 October 2025. Downloaded on 6/28/2026 1:02:36 PM.
This article is licensed under a Creative Commons Attribution 3.0 Unported Licence.

Table 3 Summary of metrics including EMD distance, tracking accuracy, and droplet average movement. EMD distance: median EMD across complete time-lapse series. Average movement: total image movement, in droplet diameter (dd) and micrometer (μm) for 30 min intervals (converted from EMD, SI Fig. S10). Percent trackable droplets: frequency calculated using previous software.[4] Accuracy: metric from tracking and parameter evaluation parameter. Trajectory accuracy output from tracking at different temporal resolutions (5 min, 15 min and 30 min). Droplets with OT scores >0.5: tracking success defined as frequency of droplets with OT-scores of all transitions x_t to $x_{t+1} > 0.5$

Metric	Small movement	Medium movement	Large movement
EMD distance	0.483	0.895	6.294
Average movement in droplet diameter (dd)	2 dd	12 dd	160 dd
μm	∼126 μm	∼800 μm	∼10 000 μm
Pixel	100 px	600 px	7700 px
Trackable by droplet centroid[5] [%]	23.2%	0.0%	0.7%
Accuracy: 5 min	0.793	0.864	0.845
Accuracy: 15 min	0.692	0.823	0.681
Accuracy: 30 min	0.682	0.750	0.617
Droplets with OT scores >0.5 [%]	91.6%	99.3%	61.8%

result in a large increase or decrease of measured fluorescence (*e.g.*, FITC-to-TRITC or FITC-to-background).

This potential interchange was calculated for every droplet-time transition and dependent on the intensity change (increase or decrease) of each droplet at time point T_x compared to T_{x-1}. First, we investigated whether we could reconstruct trajectories using barcode intensities. Indeed, the fluorescent barcodes could reproduce excellent tracking qualities and accuracies in accordance with previous data (Fig. 5). For medium movement, which is depicted in the Figure, the tracking of images with trained machine-learning approach resulted in 99% accuracy in droplet tracking with results comparable to high-temporal resolution (Fig. 5A), supporting OT-score data. Visual representation of the FITC channel intensities over time (Fig. 5B) demonstrated that only very few, distinct intensity interchanges were observed.

Finally, calculated trajectories could also be visualized in a heat-map format where droplets were mapped according to channel (barcode) and sorted according to intensity (Fig. 5C). Each line in the heatmap represents a droplet tracked over the whole time course of the experiment. Particular noteworthy was that, for tracking of droplets containing cells (DAPI, left-hand), almost no transitions were observed.

Containing cells only, high-accuracy tracking can be maintained for a sub-population of droplets

So far, all images contained cells as well as magnetic nanoparticles forming a socalled beadline as visual features. Therefore, we wondered whether our developed pipeline would also be useful for droplet array experiments that contain cells only (dataset 2). We, therefore, generated droplets containing cells only, but with fluorescent barcodes so that we could validate our approach without fine-tuning the algorithm. For this purpose, we used dataset 2, consisting of droplets containing no, one or multiple CHO cells (Fig. 6A). Here, as expected, applying the algorithm without adaption to these images led to worsening of tracking qualities, in particular for large movements in line with previous results (Fig. 6B). For low-to-medium movement, incorrectly assigned barcodes occurred in around 30% of droplets at 200 minutes of tracking and in 50% of droplets at the last time point (400 min, Fig. 6C). Still, overall, approximately 30–40% of droplets were correctly tracked without any false transitions over 400 min. Whereas not ideal, this still demonstrated success compared to previous algorithms, where low movement images could be tracked at around 20%. The loss of tracked droplets in the "low", but also "high" movement condition was attributed to movement late in the time-lapse series as indicated in the EMD profile (SI Fig. S9). Interestingly, for both experiments, droplets containing cells (labeled in blue, DAPI) were again tracked with high accuracy within the same experiment across all frames. The higher precision for cell-containing droplets was also apparent in Fig. 6B within the DAPI signal (channel with cell stain).

For large movement images (Fig. 6C), failure to track occurred in 20% of the events after 200 minutes of measurement and 40–50% at the end of the measurement caused by late, very large movement. Here, the frequency of droplets with perfect trajectories in such large-movement images was 30% at the end of the measurement. As this was only marginally weaker compared to low-to-medium movement, it indicated that movement alone did not solely predict whether the algorithm could produce accurate trajectories, but the accuracy was rather attributed to a combination of visual content, image resolution, and optimal transport.

Finally, the correlation of the uncertainty score produced by the pipeline and the occurrence of a false transition (Fig. 6D, linear regression depicted as red line with R^2 value) showed that the trajectory uncertainty score (output of the tracking model) was a good predictor and surrogate for filtering "correct" droplets. Droplets with higher uncertainty scores showed lower transitions, in line with Fig. 4. Overall, we concluded that OT tracking was able to recover substantial trajectories for low-movement conditions even in more challenging experiments. When large movement was present, OT-score filtering still permitted to retain a trackable subpopulation with correct trajectories.

Open Access Article. Published on 10 October 2025. Downloaded on 6/28/2026 1:02:36 PM.
This article is licensed under a Creative Commons Attribution 3.0 Unported Licence.

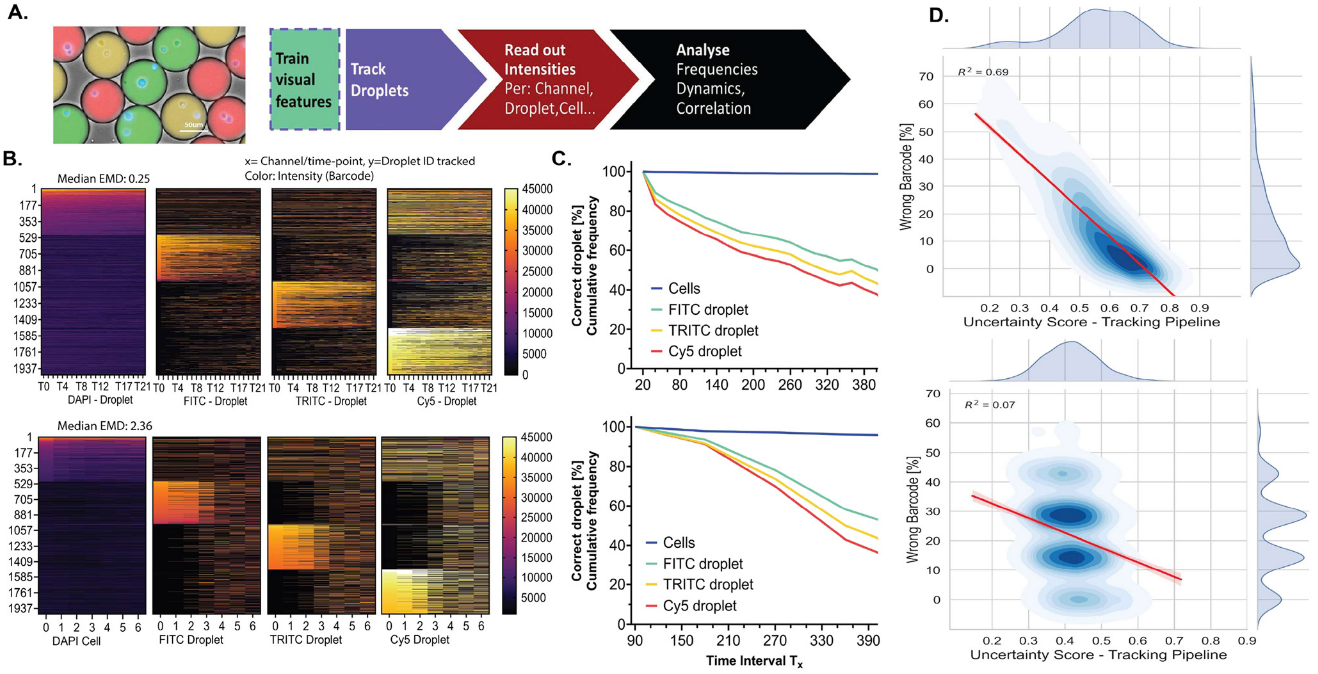

Fig. 6 CHO cell tracking and barcode analysis. Analysis of two independent experiments with color-barcoded droplets and CHO cells from experiments without additional visual features (beadline) and without prior data training, with low-to-medium movement (EMD: 0.249, upper panel) and medium-to-large movement (EMD: 2.36, lower panel). Read-out of droplet average intensity and cell signal from generated trajectories. A. Exemplary image of barcoded droplets with three droplet fluorescence dyes and DAPI-violet stained cells. Workflow for the training, tracking, read-out and analysis of biological in-droplet experiments. B. High resolution data visualization of barcode intensities (color) of individual droplet trajectories from left t_0 to right t_{final}. Per channel 500 droplets were picked at random and sorted according to fluorescence intensity in descending order for better visualization. Each line in the heat map represents a tracked droplet trajectory ID (*y*) over time (*x*). C. Cumulative frequency of successful tracking separated for each barcode channel as well as for droplets containing cells (DAPI: violet) for both movement-type images. D. Correlation between the mean uncertainty OT-score of each droplet and the percent instances that a wrong color was identified from bar-coding. The red line indicates the linear regression curve and *R*-squared value for the data correlation.

In our mouse data, visually, we observed large movement in a minority of experiments. Therefore, as expected, applying the pipeline to our mouse data consisting of 34 individual measurements did not change the number of tracked droplets for the majority of experiments (gain <15% for 27 out of 34 experiments, dataset 4), whereas a small fraction of experiments displayed large gains in droplets tracked (7 out of 34, average gain in droplets +64%). Looking at the images, four would be best classified as directional movement, two as movement due to large droplets moving into the frame displacing droplets, and one experiment that showed random movement of droplets, further illustrating different modes of potential movement modes.

Discussion

Here, we present a general workflow for the data-independent tracking of circular objects (droplets) and cells from large-scale over-time microscopic images, *i.e.*, droplet arrays. The described pipeline is the first proof-of-concept algorithm that uses unsupervised tracking of droplets containing cell and (potentially) other visual features (particles) over time and across space by using the theory of optimal transport coupled with visual feature training. The implementation of solving the OT problem for complex and disordered movement in fluidics systems of droplets provided an end-to-end pipeline for analysis. Our results suggested that, whereas classical machine-learning (visual feature training and validation), together with positional data, was sufficient for low movement conditions, more comprehensive algorithms were needed for images with larger movements (EMD >0.5) and longer time intervals. Our analysis of attraction and repulsion, along with the optimization of visual features and integration of droplet features with positional data, resulted in a comprehensive model that was also capable of dealing with larger movements above 100 droplet diameters. Investigating newly generated trajectories using low-dimensional clustering resulted in clustering of visually similar droplets from a heterogeneous population. Moreover, the success in difficult-to-track images and long time-interval instances (30 min) from previously 0–0.7% tracked droplets to 60–99.3% can be heavily attributed to the precise configuration and multi-factor integration of the pipeline. Barcode read out confirmed these results and enabled the construction of complete and correct trajectories for DAPI (Cell), FITC, TRITC, and Cy5 fluorescence intensities over time for different degree of movement. When challenging the pipeline

Open Access Article. Published on 10 October 2025. Downloaded on 6/28/2026 1:02:36 PM.
This article is licensed under a Creative Commons Attribution 3.0 Unported Licence.

with novel visual features (and the absence of nanoparticles) as in dataset 2, we could still maintain tracking for 40% in low and for 30% of droplets in high movement conditions throughout the time series without adapting the pipeline to that specific problem.

Quantitative analysis of our tracking yielded metrics such as the OT score, the accuracy of which could be confirmed as well using droplet barcodes. This metric can be used for a reliable criterion to select successfully tracked droplets. In fact, using the OT-score on dataset 2 yielded a subset of droplets which were trackable and filtered out with high certainty, demonstrating advancement also at the analysis stage. Finally, successful tracking of DAPl-stained cells across different experiments compared to droplets without cells indicates that visual features (cells inside droplets) still contributed significantly to the success. We concluded that, while optimal transport enabled more comprehensive tracking at the population level, different visual features may require re-training or calibration for instances where droplet size or cell morphology is altered and/or if other visual features (such as nanoparticles) are not present. In this context, it is important to emphasize the importance of balancing parameters between OT and visual features, as well as the role of labeling. In particular, for large movements, the pipeline required visual data inside each droplet, which was detrimental to high precision. Hence, some visual labeling may still be important when aiming to track completely novel droplet content in long-duration or high-movement experiments.

As broadness in analysis parameters came at some cost in precision for cell and droplet tracking, in the future, refining tracking models may result in even better adaptability across datasets. In fact, evaluation of movement metrics (EMD), droplet tracking quality (OT-score) and overall image quality could enable potentially automated fine-tuning of the algorithm. Such finetuning could include incorporating training to optimize the visual feature space and to set and optimize the balance between OT and visual features. Here, our published approach together with the data sets used to set up the pipeline might help researchers to develop such algorithms and benchmark these with our data.

While techniques such as optimal transport and contrastive learning have been used in other video-tracking contexts (*e.g.*, object tracking in sports videos), our work adapts these methods to the unique challenges of high-throughput, over time droplet-cell imaging. In contrast to conventional scenes with predictable motion and persistent visual context, our droplet arrays exhibit dynamic entry and exit of objects, ambiguous visual identities, and large, unpredictable movement patterns. The novelty of our pipeline lies in the integration of unbalanced optimal transport with domain-robust visual feature learning, specifically optimized for biological applications where experimental repetition is often infeasible.

Overall, these results demonstrate the robustness of our approach: even under large displacements and long intervals, the tracking model can correctly follow more than half of the population and identify a high-confidence subset with precision approaching 90%. Such performance, especially for >10× and 100× radius movements, significantly exceeds the capabilities of prior methods and enables meaningful analysis of dynamic cell behavior under challenging conditions. We believe our approach has applicability, being able to track and retrieve data from correct droplets, even in the presence of large movement, enabling more precise analysis with metrics for quantity and quality of produced trajectories and increasing throughput. Therefore, with fine-tuning parameters, our workflow could also be applied to other areas, such as for drug-organoid screening or non-droplet applications, including the tracking of extracellular vesicles or data from life-cell imaging.[32,33]

To illustrate this point, we employed the pipeline to a cohort of mice that were immunized to study the differences in humoral immunity. In this study, a small subset of datasets exhibited increased droplet movement, interestingly also different modes of movement (displacement, unidirectional, and random), which limited data extraction to only a fraction of droplets. Due to the nature of the samples and the variability between individual mice, it was not feasible to repeat the measurements without immunizing a new cohort, carrying both ethical concerns and scientific limitations. Here, the correct tracking allowed us to compare the few experiments that displayed increased movement with the others, allowing us to track the droplets and data. While frequency data would not be affected by lower droplet counts, the tracking of more droplets would allow to increase the number of events, adding more data to distributions and rare populations for analysis.

Author contributions

VB, IL and KE designed the study and supervised the project. MV, SG, TH, RD, and WO constructed the tracking pipeline workflow and simulations. AL and IL generated initial cytokine detection tracking experiments. LS generated cell experiments and constructed droplet read-out and analysis workflow. LS and MV wrote the initial draft, and all authors commented and revised the manuscript.

Conflicts of interest

K. E. holds several patents and is a scientific co-founder of Saber Bio SAS, a company developing equipment for antibody discovery. The remaining authors declare no financial or commercial conflict of interest.

Data availability

Supplementary information is available. See DOI: **https://doi.org/10.1039/D5LC00351B**.

Software is available under **https://github.com/ls154/DropletTracking**, and all other images and data will be

Open Access Article. Published on 10 October 2025. Downloaded on 6/28/2026 1:02:36 PM. This article is licensed under a Creative Commons Attribution 3.0 Unported Licence.

shared by the corresponding author upon reasonable request.

Acknowledgements

We want to acknowledge the initial algorithms for droplet, cell detection, preprocessing and visualization which were implemented by Data Science Students from the ETH AI Center - Data Science Lab 2022, namely Antoine Basseto, Francesco Da Dalt, Victor Gillioz, Samyak Jain, Filipe Cunha, Haruki Shirakami, and Yihao Liu.

References

1 J. Deguine, B. Breart, F. Lemaitre, J. P. Di Santo and P. Bousso, Intravital lmaging Reveals Distinct Dynamics for Natural Killer and CDS+ T Cells during Tumor Regression, *Immunity*, 2010, **33**(4), 632–644, DOI: **10.1016/j.immuni.2010.09.016**.

2 M. H. Robinson, N. Y. Villa, D. L. Jaye, A. K. Nooka, A. Duffy, S. S. McCachren, J. Manalo, J. M. Switchenko, S. Barnes, S. Potdar, M. I. Azeem, A. A. Horvat, V. C. Parihar, J. Gong, Y. Liang, G. H. Smith, V. A. Gupta, L. H. Boise, J. L. Kaufman, C. C. Hofmeister, N. S. Joseph, S. Lonial, K. M. Dhodapkar and M. V. Dhodapkar, Regulation of antigen-specific T cell infiltration and spatial architecture in multiple myeloma and premalignancy, *J. Clin. Invest.*, 2023, **133**(15), e167629, DOI: **10.1172/JCI167629.M**.

3 C. Toniolo, M. Delincé and J. D. McKinney, A microfluidic cell-trapping device to study dynamic host-microbe interactions at the single-cell level, *Methods Cell Biol.*, 2018, **147**, 199–213, DOI: **10.1016/bs.mcb.2018.06.008**.

4 Y. Bounab, K. Eyer, S. Dixneuf, M. Rybczynska, C. Chauvel, M. Mistretta, T. Tran, N. Aymerich, G. Chenon, J. F. Llitjos, F. Venet, G. Monneret, I. A. Gillespie, P. Cortez, V. Moucadel, A. Pachot, A. Troesch, P. Leissner, J. Textoris, J. Bibette, C. Guyard, J. Baudry, A. D. Griffiths and C. Védrine, Dynamic single-cell phenotyping of immune cells using the microfluidic platform DropMap, *Nat. Protoc.*, 2020, **15**(9), 2920–2955, DOI: **10.1038/s41596-020-0354-0**.

5 M. A. Wheeler, I. C. Clark, H. G. Lee, Z. Li, M. Linnerbauer, J. M. Rone, M. Blain, C. F. Akl, G. Piester, F. Giovannoni, M. Charabati, J. H. Lee, Y. C. Kye, J. Choi, L. M. Sanmarco, L. Srun, E. N. Chung, L. E. Flausino, B. M. Andersen, V. Rothhammer, H. Yano, T. Illouz, S. E. J. Zandee, C. Daniel, D. Artis, M. Prinz, A. R. Abate, V. K. Kuchroo, J. P. Antel, A. Prat and F. J. Quintana, Droplet-based forward genetic screening of astrocyte-microglia cross-talk, *Science*, 2023, **379**(6636), 1023–1030, DOI: **10.1126/science.abq4822**.

6 J. de Jonghe, A droplet microfluidic platform to maximise single cell sequencing information content, *Nat. Commun.*, 2023, **14**(1), 4788, DOI: **10.1038/s41467-023-40322-w**.

7 A. Pryszlak, T. Wenzel, K. W. Seitz, F. Hildebrand, E. Kartal, M. R. Cosenza, V. Benes, P. Bork and C. A. Merten, Enrichment of gut microbiome strains for cultivation-free genome sequencing using droplet microfluidics., *Cells Rep. Methods*, 2022, **2**(1), DOI: **10.1016/j.crmeth.2021.100137**.

8 A. Linder, K. Portmann and K. Eyer, The impact of cryopreservation on cytokine secretion and polyfunctionality in human PBMCs: a comparative study, *Front. Immunol.*, 2024, **7**(15), 1478311, DOI: **10.3389/fimmu.2024.1478311**.

9 K. Portmann, A. Linder, N. Oelgarth and K. Eyer, Single-cell deep phenotyping of cytokine release unmasks stimulation-specific biological signatures and distinct secretion dynamics, *Cells Rep. Methods*, 2023, **3**(7), 100502, DOI: **10.1016/j.crmeth.2023.100502**.

10 D. Wlodkowic, S. Faley, M. Zagnoni, J. P. Wikswo and J. M. Cooper, Microfluidic single-cell array cytometry for the analysis of tumor apoptosis, *Anal. Chem.*, 2009, **81**(13), 5517–5523, DOI: **10.1021/ac9008463**.

11 A. Rakszewska, J. Tel, V. Chokkalingam and W. T. S. Huck, One drop at a time: toward droplet microfluidics as a versatile tool for single cell analysis, *NPG Asia Mater.*, 2014, **6**(10), e133, DOI: **10.1038/am.2014.86**.

12 L. J. Schlotheuber, I. Lüchtefeld and K. Eyer, Antibodies, repertoires and microdevices in antibody discovery and characterization, *Lab Chip*, 2024, **24**(5), 1207–1225, DOI: **10.1039/d3lc00887h**.

13 L. G. Welch, J. Estranero, P. Tourlomousis, R. C. R. Wootton, V. Radu, C. González-Fernández, T. J. Puchtler, C. M. Murzeau, N. M. G. Dieckmann, A. Shibahara, B. W. Longbottom, C. E. Bryant and E. L. Talbot, A programmable and automated optical electrowetting-on-dielectric (oEWOD) driven platform for massively parallel and sequential processing of single cell assay operations, *Lab Chip*, 2024, **24**(16), 3763–3774.

14 A. Chakraborty and A. K. Roy-Chowdhury, Context aware spatio-temporal cell tracking in densely packed multilayer tissues, *Med. Image Anal.*, 2015, **19**(1), 149–163, DOI: **10.1016/j.media.2014.09.008**.

15 X. Bian, G. Li, C. Wang, W. Liu, X. Lin, Z. Chen, M. Cheung and X. Luo, A deep learning model for detection and tracking in high-throughput images of organoid, *Comput. Biol. Med.*, 2021, **134**, 104490, DOI: **10.1016/j.compbiomed.2021.104490**.

16 E. Moen, D. Bannon, T. Kudo, W. Graf, M. Covert and D. Van Valen, Deep learning for cellular image analysis, *Nat. Methods*, 2019, **16**(12), 1233–1246, DOI: **10.1038/s41592-019-0403-1**.

17 C. Tian, C. Yang and S. L. Spencer, EllipTrack: A Global-Local Cell-Tracking Pipeline for 2D Fluorescence Time-Lapse Microscopy, *Cell Rep.*, 2020, **32**(5), 107984, DOI: **10.1016/j.celrep.2020.107984**.

18 M. Bogdan, A. Montessori, A. Tiribocchi, F. Bonaccorso, M. Lauricella, L. Jurkiewicz, S. Succi and J. Guzowski, Stochastic Jetting and Dripping in Confined Soft Granular Flows, *Phys. Rev. Lett.*, 2022, **128**(12), 128001, DOI: **10.1103/PhysRevLett.128.128001**.

19 Y. Gai, A. Montessori, S. Succi and S. K. Y. Tang, Collective behavior of Crowded Drops in Microfluidic Systems, *Phys. Rev. Fluids*, 2022, **7**(8), 080501, DOI: **10.1103/PhysRevFluids.7.080501**.

Open Access Article. Published on 10 October 2025. Downloaded on 6/28/2026 1:02:36 PM.
This article is licensed under a Creative Commons Attribution 3.0 Unported Licence.

20 M. Durve, S. Orsini, A. Tiribocchi, A. Montessori, J. M. Tucny, M. Lauricella, A. Camposeo, D. Pisignano and S. Succi, Benchmarking YOLOv5 and YOLOv7 models with DeepSORT for droplet tracking applications, *Eur. Phys. J. E: Soft Matter Biol. Phys.*, 2023, **46**(5), 32, DOI: **10.1140/epje/s10189-023-00290-x**.

21 J. W. Pylvänäinen, E. Gómez-de-Mariscal, R. Henriques and G. Jacquemet, Live-cell imaging in the deep learning era, *Curr. Opin. Cell Biol.*, 2023, **85**, 102271, DOI: **10.1016/j.ceb.2023.102271**.

22 A. Linder, K. Portmann, L. J. Schlotheuber, A. Streuli, W. S. Glänzer, K. Eyer and I. Lüchtefeld, Microfluidic Approach to Resolve Simultaneous and Sequential Cytokine Secretion of Individual Polyfunctional Cells, *J. Visualized Exp.*, 2024, (205), e66492, DOI: **10.3791/66492**.

23 K. Abid, Hough circle transform, *GitHub*, 2013, [Online], URL: **https://github.com/abidrahmank/OpenCV2-Python-Tutorials/blob/master/source/py_turorials/py_imgproc/py_houghcircles/py_houghcircles.rst**.

24 M. A. Fischler and R. C. Bolles, Random Sample Consensus: A Paradigm for Model Fitting with Applications to Image Analysis and Automated Cartography, *Commun. ACM*, 1981, **24**(6), 381–395, DOI: **10.1145/358669.358692**.

25 M. Tan and Q. V. Le, EfficientNet: Rethinking model scaling for convolutional neural networks, *arXiv*, 2019, preprint, arXiv:1905.11946, DOI: **10.48550/arXiv.1905.11946**.

26 R. Kundu, The Beginner's Guide to Contrastive Learning, *v7labs*, 2022, Url: **https://www.v7labs.com/blog/contrastive-learning-guide**.

27 A. Van den Oord, Y. Li and O. Vinyals, Representation learning with contrastive predictive coding, *arXiv*, 2018, preprint, arXiv:1807.03748, DOI: **10.48550/arXiv.1807.03748**.

28 C. Bunne, Optimal Transport in Learning, Control, and Dynamical Systems, *ICML*, 2023, Url: **https://aimm.epfl.ch/wp-content/uploads/2023/07/script_ot_tutorial_2023.pdf**.

29 M. Cuturi, L. Meng-Papaxanthos, Y. Tian, C. Bunne, G. Davis and O. Teboul, Optimal Transport Tools (OTT): A JAX Toolbox for all things Wasserstein, *arXiv*, 2022, preprint, arXiv:2201.12324, DOI: **10.48550/arXiv.2201.12324**.

30 M. Cuturi, Sinkhorn Distances: Lightspeed Computation of Optimal Transport, *Advances in Neural Information Processing Systems*, ed. C. J. Burges, L. Bottou, M. Welling, Z. Ghahramani and K. Q. Weinberger, Curran Associates, Inc., 2013, p. 26.

31 T. Sejourne, G. Peyre and F. X. Vialard, Unbalanced optimal Transport from Theory to Numerics, *Handbook of Numerical Analysis*, ed. E. Trélat and E. Zuazua, Elsevier, 2023, vol. 24, pp. 407–471, DOI: **10.1016/bs.hna.2022.11.003**.

32 T. Staufer, C. Körnig, B. Liu, Y. Liu, C. Lanzloth, O. Schmutzler, T. Bedke, A. Machicote, W. J. Parak, N. Feliu, L. Bosurgi, S. Huber and F. Grüner, Enabling X-ray fluorescence imaging for in vivo immune cell tracking, *Sci. Rep.*, 2023, **13**(1), 11505, DOI: **10.1038/s41598-023-38536-5**.

33 J. Zhai, Y. Liu, W. Ji, X. Huang, P. Wang, Y. Li, H. Li, A. H. Wong, X. Zhou, P. Chen, L. Wang, N. Yang, C. Chen, H. Chen, P. I. Mak, C. X. Deng, R. Martins, M. Yang, T. Y. Ho, S. Yi, H. Yao and Y. Jia, Drug screening on digital microfluidics for cancer precision medicine, *Nat. Commun.*, 2024, **15**(1), 4363, DOI: **10.1038/s41467-024-48616-3**.

34 N. Aymerich, O. T. M. Bucheli, K. Portmann, L. J. Schlotheuber, I. Sigvaldadóttir, J. Baudry and K. Eyer, Non-conjugated TLR agonists increase the quantity of antibodies but not their quality in a murine immunization model, *Vaccine*, 2025, **62**, e127518, DOI: **10.1016/j.vaccine.2025.127518**.

35 N. Aymerich, O. T. M. Bucheli, K. Portmann, K. Eyer and J. Baudry, A Guide to the Quantitation of Protein Secretion Dynamics at the Single-Cell Level, *Methods Mol. Biol.*, 2024, **2804**, 141–162, DOI: **10.1007/978-1-0716-3850-7_9**.